

Low loss hybrid Nb/Au superconducting resonators for quantum circuit applications

M. C. de Ory¹, D. Rodriguez¹, M. T. Magaz¹, D. Granados², V. Rollano^{1,*}, and A. Gomez^{1,*}

¹Centro de Astrobiología (CSIC - INTA), Torrejón de Ardoz, 28850 Madrid, Spain.

²IMDEA Nanociencia, Cantoblanco, Madrid 28049, Spain

August 5, 2024

Abstract

Superconducting resonators play a crucial role in developing forthcoming quantum technologies such as quantum computing or high performance detectors. Yet, one of their main limitations regarding to noise and sensitivity is the interaction with two-level systems present in oxide layers in the device. Focused on mitigating this problem, we study a superconducting device combining a niobium circuit with a 10 nm gold capping layer. Our investigation covers a wide range of temperatures and driving powers, revealing that adding the Au layer reduces the density of two-level system defects while maintaining a very high quality factor. Moreover, an increase in the non-linearity response is also observed. Our findings suggest the potential of Nb/Au lumped element resonators as versatile and promising tools for advancing superconducting quantum technologies. Among others, the presence of gold allows anchoring alkyl thiol groups to form self-assembled monolayers, improving the integration with molecular spin qubits for the development of hybrid quantum processors.

Introduction

Superconducting microwave resonators are key building blocks in the development of different technologies with a wide range of applications including quantum computing [1], quantum communication [2], quantum sensing [3, 4] or cavities for particle accelerators [5]. These superconducting resonators stand out for their high internal quality factor (Q_i) which essentially quantifies its electromagnetic (EM) energy loss rate; a higher Q_i implies longer EM energy storage, enabling higher integration times and, thus, higher signal to noise ratio (SNR). Typically, the value of Q_i is limited by different dissipative sources including radiation losses, superconducting vortices or residual surface resistance, among others [6, 7]. In the single photon and low-temperature limits, Q_i is predominantly limited by the parasitic noise generated by two-level systems (TLSs) developed via trapped charges and electric dipoles naturally present in amorphous dielectric layers in contact with the superconductor, such as native oxides at its surface or the substrate/superconductor interface. TLSs couple to the resonator electric field [8, 9], inducing non-desired energy dissipation and decoherence, lowering, and thus degrading the device performance. Therefore, reducing or even eliminating TLSs is a must to attain better control of the microwave losses and boost the resonator performance.

In this sense, ongoing research continues into developing resonators with reduced TLS noise [10]. Different strategies have been approached, including the optimization of the nanofabrication processes [11], substrate choice [12], surface treatment [13], resonator design [14, 15], or the use of different superconducting materials [12, 16, 17]. Typical superconducting materials employed for developing high-quality resonators include niobium (Nb) or aluminum (Al), depending on the application. For instance, Al is widely used to develop Kinetic Inductance Detectors, state-of-the-art radiation detectors typ-

ically used for astrophysics experiments [18]. On the other hand, Nb resonators are preferred for quantum computing applications, as their higher critical temperature ($T_c \sim 9$ K) and larger critical field lead to better stability against temperature and magnetic field fluctuations. Furthermore, this resilience makes them suitable for quantum applications requiring magnetic fields, opening the path for the implementation of new hybrid quantum architectures based on molecular spins qubits [19, 20] or magnonic excitations [21, 22]. Even though these materials have proven to have very high performance, their internal quality factor is still limited by the noise generated by the TLSs present in the native oxide layer, among others [23]. In this work, we propose using bilayer niobium/gold (Nb/Au) Lumped Element Resonators (LERs). The thin gold layer deposited on top of the niobium film prevents oxidation, enhancing surface stability and reducing the density of TLSs. Thus, the presence of the Au layer contributes to increase the internal quality factor and performance reliability of the resonators. Beyond its role in preserving oxidation of the Nb surfaces, the Au layer also offers advantages in quantum computing and sensing technologies. On one hand, using the Au thickness as a design criterion, the Au capping layer enables controlling L_k through proximity effect [24, 25]. This parameter relates to the inertia of the superconducting charge carriers when an alternating current is applied and, distinct from its geometric counterpart, it exhibits a strong dependence on current and temperature. This characteristic leads to enhanced responsivity in detectors [26], allows for the tunability of resonance frequency [27] and is suitable for development parametric amplifiers [28]. The kinetic inductance contribution also increases the characteristic impedance and, therefore, the zero-point voltage fluctuations, making it an ideal platform for efficiently coupling microwave photons to small electric dipole moments [29]. On the other hand, the integration of molecular systems for the development of an hybrid quantum processor based on molecular-based qu-

* Corresponding authors: vrollano@cab.inta-csic.es, agomez@cab.inta-csic.es

dits [20] also remains a challenge. In fact, the presence of a gap between the resonator and the molecular ensemble crystal wastes the region of the resonator mode volume where the electromagnetic fields are more intense [19]. An Au capping layer, as the one proposed here, may serve as an alternative for this integration using self-assembled monolayers (SAMs), which can be anchored to the Au surface via thiol groups [30, 31]. This characteristic enables reducing the gap to zero, exploiting the highest microwave magnetic field intensity close to the resonator surface and, thereby, maximizing the coupling strength with the molecules. Finally, the native oxide of the superconductor surface is a significant obstacle when applying these devices to applications involving scanning tunnelling microscopy (STM) [32]. In this bilayer design, the Au layer improves the performance of the device in STM conditions, avoiding the native oxide, which, together with the possibility of SAMs deposition, opens the door to coherent control of spin qubits on sur-

faces using Nb superconducting resonators [33, 34]. Moreover, recent studies have shown that using the Nb/Au proximitized film could help increase the spin-based qubits' lifetime [35]. Here, the experimental demonstration of Nb/Au superconducting LERs and its comparison with bare Nb ones is presented. Microwave characterization shows a systematic increase in the internal quality factor, reaching up to 1M, and a reduction of the TLS density when adding the Au as a protective layer opening the possibility for its use in superconducting quantum circuits applications.

The paper is organized as follows: the methods section describes the superconducting chips and explains the fabrication and characterization processes. Then, in the results and discussions section we explore the influence of TLS in the resonator parameters as a function of temperature and driving power. A final section summarizes our results and explores further appli-

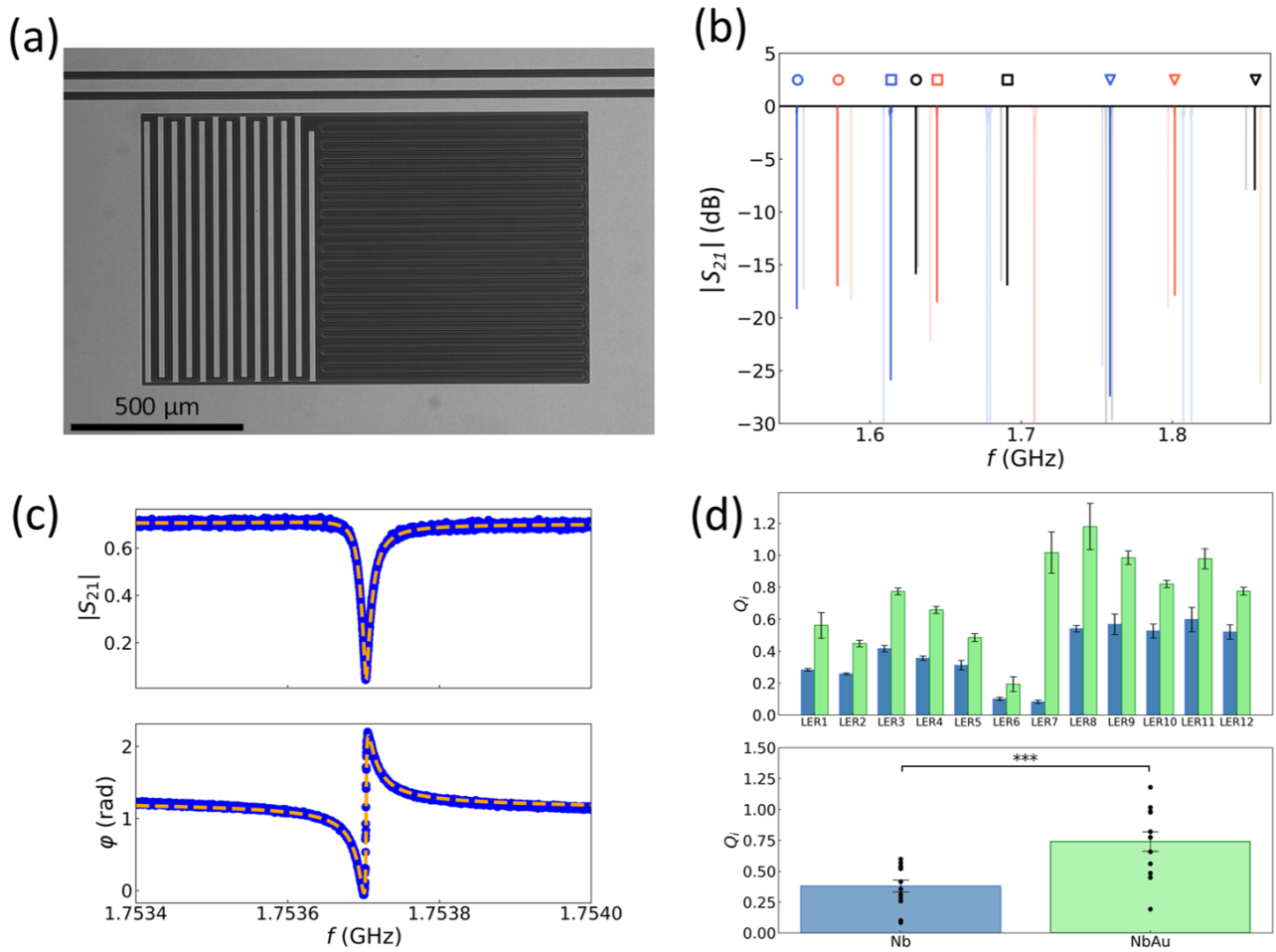


Figure 1. (a) Optical image of one of the fabricated Nb/Au LERs. (b) Amplitude of the transmission as a function of frequency measured for the twelve LERs on each chip. Measurements for the Nb/Au and Nb devices are shown in blue and red, respectively. The simulated resonances considering $L_k = 0$ pH/sq are depicted in black. Highlighted traces show the LERs resonances that are studied in detail for the rest of the article. Symbols above these resonances indicate which ones share the same LER geometry: LER1 design is represented by circles, LER4 by squares and LER8 by triangles. These symbols will be consistently used in subsequent figures. (c) Amplitude (top) and phase (bottom) of the transmission as a function of frequency obtained for the Nb/Au LER8 resonator at 15 mK with a driving power of -96 dBm. Blue dots show the experimental data, while orange dashed lines show the fit obtained using Equation (1). Parameter values resulting from the fit are $f_r = 1.7537$ GHz, $Q_i = (1.48 \pm 0.14) \cdot 10^6$ and $Q_c = (7.90 \pm 0.08) \cdot 10^4$. (d) Top: Internal quality factor as a function of LER number for Nb (green) and Nb/Au (blue). Bottom: Results of a paired t-test performed on the two Q_i distributions. The Q_i values correspond to a driving power of -100 dBm. The analysis yields a p-value of 0.0002 (represented by the three stars in the plot).

Methods

A superconducting Nb/Au chip together with a nominally identical base Nb chip as control sample have been developed. Each chip contains twelve LERs, which are coupled in parallel to a single coplanar waveguide transmission line (CPW) that serves for microwave readout. Resonators are labeled sequentially from LER1 to LER12, with higher labels corresponding to higher resonance frequency values. The LERs designs have been modeled through electromagnetic simulations using Sonnet Suite software [36]. The resonance frequency is given by $f_r = 1/2\pi\sqrt{LC}$, where L is the inductance and C the capacitance of each resonator. The three of them are designed with the same inductor L , so their resonance frequency is set by changing the area of the capacitor, hence modifying the value of C . The CPW line is matched to a $50\ \Omega$ impedance, with a center conductor of $40\ \mu\text{m}$ width separated $20\ \mu\text{m}$ from the ground planes. The coupling quality factor (Q_c) is set by the distances between the LER and the CPW and ground planes.

The device fabrication process starts with the surface preparation of a $270\ \mu\text{m}$ high-resistivity silicon (Si) substrate ($R > 1\ \text{k}\Omega\cdot\text{cm}$), using a 1% hydrofluoric acid bath to remove the native silicon oxide from the wafer. Immediately afterwards, the sample is introduced in an electron-beam evaporator where the three layers, Ti 2.5 nm / Nb 100 nm / Au 10 nm, are deposited. In the case of the bare Nb resonators, Ti 2.5 nm / Nb 100 nm are evaporated in an independent procedure. In both cases, the titanium (Ti) seed layer is used to improve the adhesion to Si substrate. The patterning process is based on maskless laser-writer photolithography using AZnLOF 2070 negative photoresist. Afterwards, the etching process is performed in three steps: first, the gold film is etched by argon ion milling, then the niobium film is removed using a SF₆:Ar plasma etching and, finally, the Ti is removed using wet etching. The remaining resist is removed in acetone and isopropanol rinse and RF oxygen plasma cleaner. Figure 1a shows an optical image of one fabricated Nb/Au LER as an example.

The devices are cooled down to millikelvin temperatures using a dilution refrigerator (Bluefors LD250), while the electrodynamic response is measured with a commercial Vector Network Analyzer (VNA). The input power is varied from $-60\ \text{dBm}$ to $+20\ \text{dBm}$ from the VNA and attenuated by 30 dB at room temperature, 20 dB in the 4 K stage and 10 dB in the 100 mK stage.

DC blocks prevent DC current leakages and provide thermal breaks between stages. The output signal is then amplified by a low-noise amplifier at the 4 K stage and a second amplification stage outside the refrigerator. Stainless steel (SS), CuNi and (superconducting) NbTi cables are used between stages in order to guarantee good electrical conductivity and poor thermal conductivity, whilst copper cables are used to thermalize within the stage. The final devices are mounted in a cold finger in the mixing chamber plate on a superconducting aluminum holder with a PCB, using low temperature varnish (SCBltv01) for thermalization and aluminum wire-bonding for electrical connections. The sample is further magnetically screened using a mu-metal shield at room temperature.

Results and discussion

In Figure 1(b), we present the amplitude of the transmission parameter $|S_{21}|$ as a function of frequency for the twelve LERs on each chip. The data for Nb is shown in red and for Nb/Au in blue, both measured at 15 mK with a driving power of $-96\ \text{dBm}$. Each resonance appears as a dip in the transmission spectrum. In this figure there are highlighted three resonances per chip, corresponding to resonators LER1, LER4, and LER8, indicating that their properties will be examined in detail later in the article. For comparison, the simulated transmission considering a perfect conductor (with $L_k = 0\ \text{pH/sq}$) is also plotted. Figure 1(c) illustrates the complex transmission spectrum (both amplitude and phase) at 15 mK, driven by an input signal of $-96\ \text{dBm}$ for one of these three Nb/Au LERs as an example. The transmission parameter of a resonator can be modeled as follows:

$$S_{21} = a \left[1 - \frac{\frac{Q_l}{Q_c}}{1 + 2iQ_l \left(\frac{f-f_r}{f_r} \right)} \right] \quad (1)$$

where the loaded quality factor (Q_l) is $Q_l^{-1} = Q_i^{-1} + Q_c^{-1}$. We fit the resonance data using the method detailed in [37], obtaining the resonator parameters f_r , Q_i , and Q_c . The fitting result is shown in figure 1(c) with orange dashed lines.

The comparison of the transmission spectra for Nb/Au and Nb LERs reveals a systematic shift to lower resonance frequencies (f_r) when adding the Au layer (see figure 1(b)). This behavior

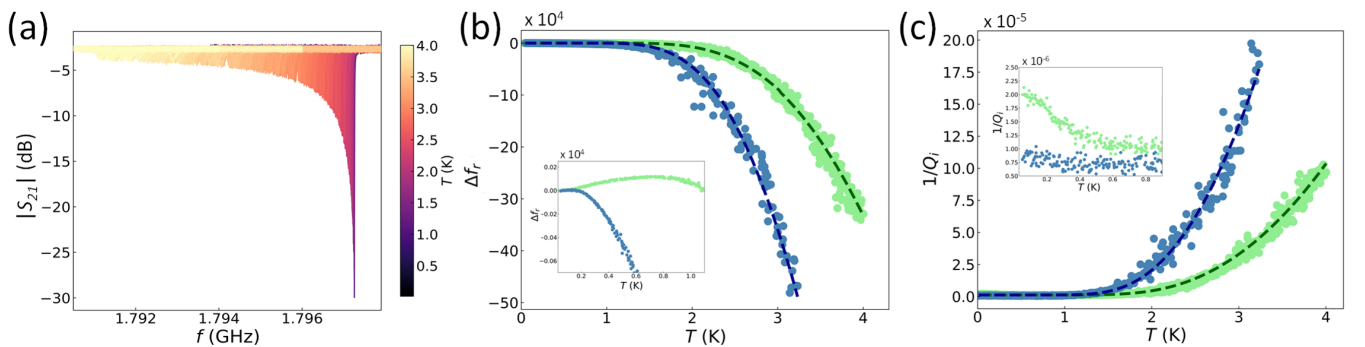


Figure 2. (a) Amplitude of the transmission spectrum in dB as a function of temperature for one Nb resonator measured with a driving amplitude of $-92\ \text{dBm}$. Color scale indicates the chip temperature. (b) Fractional change of the resonance frequency as a function of the chip temperature for a Nb/Au resonator (light blue) and a Nb resonator (light green). Dashed lines depict the Mattis-Bardeen fit upon the experimental data. Nb/Au fit is shown in dark blue while Nb fit is shown in dark green. Inset shows in detail the low-temperature regime. (c) Inverse of the internal quality factor as a function of temperature in the low temperature regime for Nb and Nb/Au. Color scheme is the same as in panel (b). Inset shows in detail the low-temperature regime.

may be attributed to an excess of quasiparticles scattered at the boundary between the two materials, which leads to an increase in the kinetic inductance (L_k) [38]. From the experimental results, L_k is determined for both materials by comparing the measured resonance frequencies (f_{meas}) with the simulated ones, using this expression:

$$L_k = \left[\left(\frac{f_{sim}}{f_{meas}} \right)^2 - 1 \right] L_g \quad (2)$$

where f_{sim} is the resonance frequency of the simulated resonator ($L_k = 0$ pH·sq⁻¹) and L_g is the geometric inductance, which is consistent across the three resonators due to their identical inductor lengths. The calculated mean value is $\bar{L}_k = 0.13 \pm 0.01$ pH/sq for the Nb resonators and $\bar{L}_k = 0.22 \pm 0.02$ pH/sq for the Nb/Au ones. Subsequently, the kinetic fraction (α_k), defined as L_k over the total inductance ($L_g + L_k$), can be obtained. Results show that Nb/Au resonators exhibit a higher α_k , being the mean values $\bar{\alpha}_k = 0.057 \pm 0.005$ for Nb and $\bar{\alpha}_k = 0.094 \pm 0.005$ for Nb/Au. The parameter α_k is critical in developing kinetic inductance detectors; a higher α_k enhances device device responsivity [39]. Additionally, a higher α_k leads to increased frequency tunability and amplification in superconducting devices developed for quantum applications [27, 28].

A statistical analysis of the Q_i values obtained from fitting the complex transmission measured at -100 dBm for the twelve LERs and both materials is presented in figure 1(d). The upper plot compares each pair of LERs (corresponding to the same design), and illustrates that NbAu LERs consistently exhibit a higher internal quality factor. The lower plot contrasts the average Q_i value for all LERs between the two materials. The paired t-test made upon the two groups of LERs provides a strong statistical evidence that there is a significant difference between the two groups of resonators when comparing the internal quality factors. From now on, we will analyze the physical properties of the aforementioned three LER designs (see figure 1(b)), focusing on the loss mechanisms that affect the internal quality factor of the resonators.

Temperature sweeps were conducted for LER8 fabricated of both materials. Figure 2(a) shows the amplitude of the transmission spectrum as a function of the chip temperature (T)

measured from 15 mK to 4 K for the Nb LER8 as an example. The measurements were performed with a low driving power (-92 dBm), where the TLSs are not expected to saturate. As temperature increases, the peak broadens while the resonance frequency shifts towards lower values due to the gradual deterioration of the superconducting properties in the material. The peak broadening relates to the losses of the resonator, while the change in the resonance frequency results from the increased kinetic inductance of the Cooper pairs in the superconducting material. The fitting procedure, using equation (1) on the data presented as explained, allows us to determine f_r and Q_i as a function of temperature. Figure 2(b) displays the fractional change in resonance frequency (Δf_r) for both materials as a function of temperature, given by $\Delta f_r(T) = (f_r(T) - f_{r,0})/f_{r,0}$. Here, $f_{r,0}$ is the resonance frequency at the lowest measured temperature (15 mK), at which the superconducting properties of the device are fully recovered. Figure 2(c) depicts the inverse of the internal quality factor as a function of temperature, which is proportional to the losses of the superconducting material. The ideal electromagnetic response of a superconductor is described by the Mattis-Bardeen (MB) model by using a complex conductivity $\sigma_s = \sigma_1 - i\sigma_2$ where the real part characterizes the dissipative processes while the imaginary part accounts for the inductive response of the superconductor. Specifically, σ_1 describes the behaviour of the quasiparticles while σ_2 relates to the Cooper pairs of the condensate. The model explains how f_r and Q_i depend on the complex conductivity:

$$\Delta f_r^{MB}(T) = \frac{\alpha_k}{2} \Delta \sigma_2(T) \quad (3)$$

and,

$$Q_i^{-1}(T) = \alpha_k \frac{\sigma_1(T)}{\sigma_2(T)} \quad (4)$$

Figures 2(b) and 2(c) show in dashed lines the fits obtained from MB model using Equations (3) and (4). The analysis was performed assuming a temperature-dependent superconducting gap [40]. In the high-temperature regime, the onset of dissipative behaviour corresponds to $T \sim T_c/5$, which is in good agreement with the MB model [41]. The values extracted from the fits for this LER are $\alpha_k(Nb) = 0.063 \pm 0.006$ with

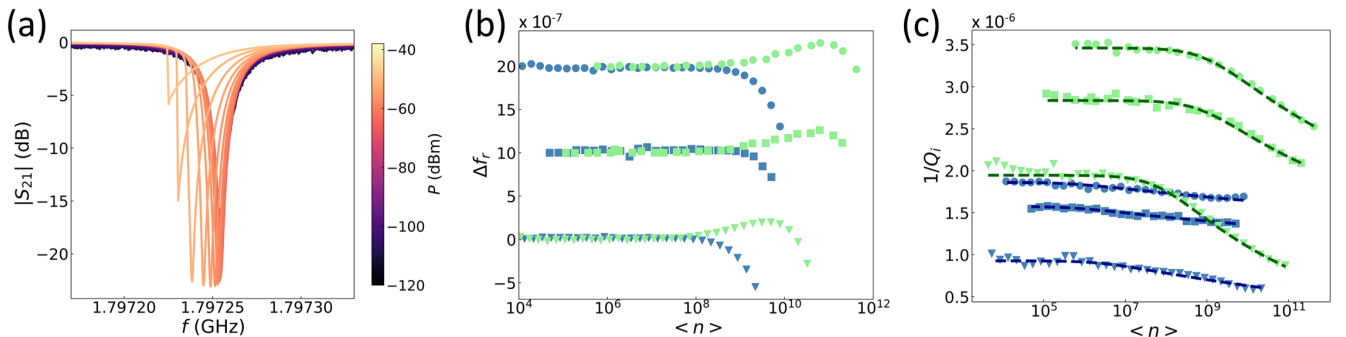


Figure 3. (a) Transmission spectra as a function of driving power for the Nb LER8 resonator measured at 15 mK. (b) Fractional resonance frequency shift as a function of photon number for the Nb resonators (light green) and the Nb/Au ones (light blue). The photon number is obtained from Equation (5). Symbols represent the results for the different designs, circles for LER1, squares for LER4, and triangles for LER8. For clarity, the data corresponding to LER1 and LER4 has been upshifted +20 and +10 units respectively. (c) Inverse of the internal quality factor ($\tan \delta$) as a function of the number of photons in the resonator. Experimental data in light green circles for Nb and light blue for Nb/Au. Dashed lines (dark green for Nb and dark blue for Nb/Au) show the fits performed using Equation (6) upon the experimental data.

LER# (material)	n_c	β	$F \cdot \delta_{TLS}^0$	Q_i^{sat}	f_r (GHz)
LER1 (Nb)	$(1.02 \pm 0.11) \cdot 10^9$	$(8.46 \pm 1.73) \cdot 10^{-2}$	$(2.48 \pm 0.37) \cdot 10^{-6}$	$(8.80 \pm 0.66) \cdot 10^5$	1.578422
LER1 (Nb/Au)	$(4.41 \pm 1.72) \cdot 10^5$	$(3.05 \pm 1.31) \cdot 10^{-2}$	$(8.77 \pm 4.05) \cdot 10^{-7}$	$(9.64 \pm 1.21) \cdot 10^5$	1.551530
LER4 (Nb)	$(7.46 \pm 0.89) \cdot 10^8$	$(1.14 \pm 0.25) \cdot 10^{-1}$	$(1.81 \pm 0.34) \cdot 10^{-6}$	$(8.72 \pm 0.67) \cdot 10^5$	1.644296
LER4 (Nb/Au)	$(3.40 \pm 1.02) \cdot 10^6$	$(4.81 \pm 2.46) \cdot 10^{-2}$	$(6.07 \pm 2.46) \cdot 10^{-7}$	$(9.99 \pm 1.15) \cdot 10^5$	1.613699
LER8 (Nb)	$(6.93 \pm 0.51) \cdot 10^7$	$(1.15 \pm 0.12) \cdot 10^{-1}$	$(1.97 \pm 0.59) \cdot 10^{-6}$	$(9.52 \pm 0.69) \cdot 10^5$	1.797254
LER8 (Nb/Au)	$(2.59 \pm 0.91) \cdot 10^6$	$(4.65 \pm 2.58) \cdot 10^{-2}$	$(9.74 \pm 4.08) \cdot 10^{-7}$	$(9.91 \pm 1.09) \cdot 10^5$	1.753702

Table 1. Parameters obtained from fit upon experimental data shown in Figure 4 using Equation (6). Last column shows the resonance frequency f_r of each resonator obtained from fitting the complex trace using equation (1) in the low power regime with a driving power of -99 dBm. Error in resonance frequency is lower than 10^{-4} percent.

$T_c(Nb) = 8.7 \pm 0.2$ K, whereas $\alpha_k(Nb/Au) = 0.103 \pm 0.015$ with $T_c(Nb/Au) = 7.3 \pm 0.3$ K. These results are in good agreement with the α_k values obtained from the comparison made using equation (2). The reduction of T_c and the increase of α observed in the Nb/Au can be attributed to the proximity effect, which comes along with an excess of quasiparticles introduced by the Au layer in the interface [38, 42].

As can be seen in the inset of figure 2(b), in the low-temperature regime the behavior of the resonance frequency with temperature differs between the two materials. For the Nb device, Δf_r exhibits an upshift as temperature rises, while for the Nb/Au resonator it presents a quick drop with no upshift. This trend in the resonance frequency translates into an increase in Q_i^{-1} for Nb at low temperatures which is not observed in Nb/Au. The difference between the two materials may be consequence of the thermal saturation of the TLSs for $T_{bath} = hf/2k_B$ [43]. As temperature increases, the upper energy level of the TLSs gets populated, decreasing the losses of the resonator towards them and hence increasing Q_i . This is not observed for the Nb/Au resonator, for which Q_i remains constant up to $T \sim 1.5$ K, revealing that microwave losses are not TLS limited in the case of Nb/Au.

To further investigate the nature of the loss mechanism in the devices, we have characterized the TLS contribution as a function of the driving power at 15 mK, where the condition $hf > 2k_B T$ is met and the thermal desaturation results in a power dependent resonator loss rate. As an example, figure 3(a) shows the transmission spectra of a single Nb LER measured at different driving powers, ranging from -120 dBm to -40 dBm. From these values, the average number of photons in the resonator can be estimated using:

$$n = \frac{Q_i^2}{Q_c \pi} \frac{P_d}{hf_r^2} \quad (5)$$

Figure 3(b) shows Δf_r as a function of the number of photons for the three LERs and both materials, measured at 15 mK. For the Nb resonators we observe a positive resonance shift as n increases, which can be attributed to the gradual saturation of the resonant TLSs. In the case of the Nb/Au resonators, this upshift is not observed which may be attributed to a low TLSs density. For higher values of n , the nonlinearity of the kinetic inductance dominates the physics of the system when the current density (J) in the resonator reaches a value J^* , which sets the scale of the nonlinearity in the superconductor and it is close to the critical current density of the superconducting material [44]. As consequence, both LERs develop a strong asymmetric resonance response, which translates into a sharp jump in the transmission spectra and a negative relative frequency shift (see

figure 3(a) as an example).

The inverse of the internal quality factor as a function of n at 15 mK is shown in figure 3(c). Consistently, an overall enhancement of the Q_i is obtained for the Nb/Au resonators in comparison with the Nb ones. Beyond a critical number of photons (n_c), a steeper dependence of the microwave losses (Q_i^{-1}) with n is observed in the Nb LERs with respect the Nb/Au ones. This decrease in Q_i^{-1} originates in the competition between the driving power and the relaxation (γ_1) and decoherence rates (γ_2) of the resonant TLSs. The value of n_c is reached when the amplitude of the driving signal (i.e, the Rabi frequency $\Omega_R \sim n^{1/2}$) increases beyond the TLSs loss rate $\sqrt{\gamma_1 \cdot \gamma_2}$, since more of them are being locked onto their excited state [45]. Hence, resonant TLSs can absorb gradually less energy from the resonator and their contribution to the internal quality factor decreases. This behaviour can be modeled using the following expression [15]:

$$\frac{1}{Q_i} = \tan \delta = F \cdot \delta_{TLS}^0 \frac{\tanh\left(\frac{hf_r}{2k_B T}\right)}{\left(1 + \frac{\langle n \rangle}{n_c}\right)^\beta} + \frac{1}{Q_i^{sat}} \quad (6)$$

Where F is the ratio between the volume of the electric field coupled to the TLSs and the entire electric field volume created by the resonator, δ_{TLS}^0 is the loss tangent associated to the resonant TLSs density in the low temperature and photon limits, β is an exponent that describes how strongly Q_i depends on the photon number, and $1/Q_i^{sat}$ is the high-power loss, for which the resonant TLSs are saturated and other loss mechanisms dominate [17, 42]. Dashed lines in figure 3(c) show the obtained fit made upon the experimental using the previous model. Table 1 compiles the values obtained from these fits. For the Nb resonators, the critical photon numbers are in the order of 10^8 , which are usually attributed to the contribution of the Nb₂O₅ oxide [23]. Conversely, their Nb/Au counterparts show n_c values of about two orders of magnitude lower, which may be ascribed to the lower number of photons required to saturate the TLSs coupled to the capacitor due to the Au layer. Moreover, the loss tangent value ($F \delta_{TLS}^0$) obtained for the Nb/Au resonators are systematically lower when compared with the Nb ones. Finally, for both materials, a weak dependence of Q_i^{-1} with the number of photons ($\beta \sim 0.1$) implies a strong TLS - TLS interaction, which is typical from Nb₂O₅ [23, 42]; however, the analysis shows a weakened dependence induced by the presence of the Au layer, as evidenced by a smaller β in Nb/Au resonators.

These results endorse the idea that Nb/Au resonators present a lower TLS density coupled to them, since the Au layer prevents the growth of Nb₂O₅. Nevertheless, the critical photon

numbers obtained for Nb/Au are not low enough to associate the resonators loss to the Si substrate native oxide. Some Nb oxide can still be present in the lateral areas of the superconductor, which are exposed after the etching process, explaining why the photon number is not even lower in Nb/Au. Under low driving power conditions, where TLS contributions are predominant, Nb/Au resonators display internal quality factors that are approximately twice of those observed in the Nb resonators. The $F\delta_{TLS}^0$ values for Nb, consistent with previous reports [14], exceed those for Nb/Au, indicating a reduced impact of TLSs in the latter. At the high-power regime, the values obtained for Q_i^{sat} are similar for both materials, suggesting that the loss mechanism when the TLSs are saturated may have the same origin.

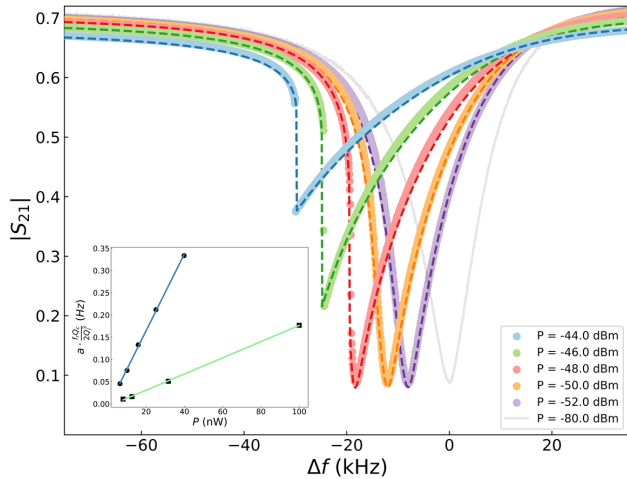


Figure 4. Amplitude of the transmission as a function of frequency for the Nb/Au resonator LER1 with driving powers between -44 dBm and -52 dBm. Dark-colored dashed lines correspond to the fit made using the non-linear model. Light gray curve represents the resonance data measured at low driving power (-80 dBm). The horizontal axis is referenced to the resonance frequency in the low-power regime ($f_{r,0}$). The inset shows the non-linearity parameter a as a function of driving power (in linear scale) for both Nb and Nb/Au, along with the corresponding linear fit results in green and blue respectively.

Finally, we have investigated the effect of the Au layer on the kinetic inductance of the resonators by determining the current density value in the inductor that marks the onset of non-linear behaviour (J^*). Figure 4 shows several transmission spectra at high driving powers (between -44 dBm and -52 dBm) for the Nb/Au resonator LER1. As the resonance shifts towards lower frequencies, a feature already shown in figure 3, it develops a strong asymmetric profile and shows discontinuities since the current in the inductor of the resonator increases. In the non-linear regime, the resonance model used to fit the experimental data is described in reference [44]. In this model, the parameter a describes the strength of the non-linearity for a given driving power (P_d):

$$a = \frac{2Q^3 P_d}{Q_c f_r E_*} \quad (7)$$

where E_* represents the energy scale at which the resonator physics starts to be dominated by the non-linearity. We obtained the parameter a as a function on P_d , as shown in the inset of figure 4. The slope of this linear relation gives the value of E_* . Then, E_* and J_* are related through $E_* \propto L_k J_*^2 / \alpha$. By analyzing the data for both materials in this way, we obtain that the

nonlinear regime begins at $J^* = (1.54 \pm 0.22) \cdot 10^9 \text{ A} \cdot \text{cm}^{-2}$ for Nb and $J^* = (6.93 \pm 0.35) \cdot 10^8 \text{ A} \cdot \text{cm}^{-2}$ for Nb/Au. This reduction in J^* is likely originated in the excess of quasiparticles introduced by the Au layer, leading to an enhance tunability of the devices, and useful for further applications.

Conclusions

In summary, we have fabricated superconducting lumped element resonators made of an Nb/Au bilayer and characterized their properties (resonance frequency and internal quality factor) as a function of temperature and driving power. We have compared our results by performing the same experiments in a nominally identical control sample fabricated of bare Nb. The microwave characterization in our Nb/Au and Nb devices matches our simulated designs in a consistent manner, proving a reliable manufacturing process. Adding the Au layer avoids Nb oxidation and reduces TLS loss while increasing the kinetic inductance of the device. Furthermore, we obtain internal quality factors higher than 1M for the Nb/Au devices even when the TLSs are not saturated, proving that the Au capping layer does not spoil the resonator properties but actually improves them. Overall, our results show that Nb/Au superconducting LERs outperform the bare Nb ones with reference to the internal quality factor, TLS contribution and responsivity with a direct impact in the applicability of these resonators. In particular, these devices may allow an optimized integration of molecular spin-based quantum devices thanks to the ease of functionalizing the Au layer and open new possibilities in STM experiments. In addition, the higher kinetic inductance and an increase nonlinearity in the Nb/Au devices make them more suitable to be applied as kinetic inductance parametric amplifiers, tunable resonators or single photon detectors.

Acknowledgments

This work has received support from grants TED2021-131447B-C22, PID2022-137779OB-C41, PID2022-137779OB-C42 and the research network RED2022-134839-T funded by the Spanish MCIN/AEI/10.13039/501100011033, by the EU “NextGenerationEU”/PRTR and by the “ERDF A way of making Europe”. IMDEA Nanoscience acknowledges financial support from the “Severo Ochoa” Programme for Centres of Excellence in R&D (CEX2020-001039-S) and CAB from the the CSIC Research Platform PTI-001 and from “Tecnologías avanzadas para la exploración del Universo y sus componentes” (PR47/21 TAU-CM) project funded by Com. de Madrid, by “NextGenerationEU”/PRTR.

References

- Blais, A., Huang, R.-S., Wallraff, A., Girvin, S. M. & Schoelkopf, R. J. Cavity quantum electrodynamics for superconducting electrical circuits: An architecture for quantum computation. *Phys. Rev. A* **69**, 062320 (6 June 2004).
- Rosario, P., Santos, A. C., Villas-Boas, C. & Bachelard, R. Collateral Coupling between Superconducting Resonators: Fast High-Fidelity Generation of Qudit-Qudit Entanglement. *Phys. Rev. Appl.* **20**, 034036 (3 Sept. 2023).
- Weichselbaumer, S. *et al.* Quantitative modeling of superconducting planar resonators for electron spin resonance. *Physical Review Applied* **12**, 024021 (2019).

4. Baselmans, J. *et al.* Ultra-sensitive THz microwave kinetic inductance detectors for future space telescopes. *Astronomy & Astrophysics* **665**, A17 (2022).
5. Padamsee, H. S. Superconducting radio-frequency cavities. *Annual review of nuclear and particle science* **64**, 175–196 (2014).
6. Gurevich, A. V. Tuning microwave losses in superconducting resonators. *Superconductor Science and Technology* **36**, 063002 (2023).
7. Krasnok, A. *et al.* Advancements in Superconducting Microwave Cavities and Qubits for Quantum Information Systems. *arXiv preprint arXiv:2304.09345* (2023).
8. Pappas, D. P., Vissers, M. R., Wisbey, D. S., Kline, J. S. & Gao, J. Two level system loss in superconducting microwave resonators. *IEEE Transactions on Applied Superconductivity* **21**, 871–874 (2011).
9. Martinis, J. M. *et al.* Decoherence in Josephson qubits from dielectric loss. *Physical review letters* **95**, 210503 (2005).
10. Béjanin, J. *et al.* Fluctuation spectroscopy of two-level systems in superconducting resonators. *Physical Review Applied* **18**, 034009 (2022).
11. Barends, R. *et al.* Reduced frequency noise in superconducting resonators. *Applied Physics Letters* **97**, 033507 (July 2010).
12. Barends, R. *et al.* Noise in NbTiN, Al, and Ta Superconducting Resonators on Silicon and Sapphire Substrates. *IEEE Transactions on Applied Superconductivity* **19**, 936–939 (2009).
13. Bruno, A. *et al.* Reducing intrinsic loss in superconducting resonators by surface treatment and deep etching of silicon substrates. *Applied Physics Letters* **106**, 182601 (May 2015).
14. Gao, J. *et al.* Experimental evidence for a surface distribution of two-level systems in superconducting lithographed microwave resonators. *Applied Physics Letters* **92**, 152505 (Apr. 2008).
15. McRae, C. R. H. *et al.* Dielectric loss extraction for superconducting microwave resonators. *Applied Physics Letters* **116** (2020).
16. Barends, R. *et al.* Minimal resonator loss for circuit quantum electrodynamics. *Applied Physics Letters* **97**, 023508 (July 2010).
17. McRae, C. R. H. *et al.* Materials loss measurements using superconducting microwave resonators. *Review of Scientific Instruments* **91** (2020).
18. Baselmans, J. Kinetic inductance detectors. *Journal of Low Temperature Physics* **167**, 292–304 (2012).
19. Rollano, V. *et al.* High cooperativity coupling to nuclear spins on a circuit quantum electrodynamics architecture. *Communications Physics* **5**, 246 (2022).
20. Chiesa, A. *et al.* Blueprint for a Molecular-Spin Quantum Processor. *Physical Review Applied* **19**, 064060 (2023).
21. Tabuchi, Y. *et al.* Hybridizing ferromagnetic magnons and microwave photons in the quantum limit. *Physical review letters* **113**, 083603 (2014).
22. Pirro, P., Vasyuchka, V. I., Serga, A. A. & Hillebrands, B. Advances in coherent magnonics. *Nature Reviews Materials* **6**, 1114–1135 (2021).
23. Verjauw, J. *et al.* Investigation of microwave loss induced by oxide regrowth in high-Q niobium resonators. *Physical Review Applied* **16**, 014018 (2021).
24. Guéron, S., Pothier, H., Birge, N. O., Esteve, D. & Devoret, M. Superconducting proximity effect probed on a mesoscopic length scale. *Physical review letters* **77**, 3025 (1996).
25. Hu, J. *et al.* Proximity-coupled Al/Au bilayer kinetic inductance detectors. *Journal of Low Temperature Physics* **199**, 355–361 (2020).
26. Valenti, F. *et al.* Interplay between kinetic inductance, nonlinearity, and quasiparticle dynamics in granular aluminum microwave kinetic inductance detectors. *Physical review applied* **11**, 054087 (2019).
27. Vissers, M. R. *et al.* Frequency-tunable superconducting resonators via nonlinear kinetic inductance. *Applied Physics Letters* **107** (2015).
28. Chien, W.-C. *et al.* Large parametric amplification in kinetic inductance dominant resonators based on 3 nm-thick epitaxial superconductors. *Materials for Quantum Technology* **3**, 025005 (2023).
29. Samkharadze, N. *et al.* High-kinetic-inductance superconducting nanowire resonators for circuit QED in a magnetic field. *Physical Review Applied* **5**, 044004 (2016).
30. Cornia, A., Mannini, M., Sainctavit, P. & Sessoli, R. Chemical strategies and characterization tools for the organization of single molecule magnets on surfaces. *Chemical Society Reviews* **40**, 3076–3091 (2011).
31. Gabarró-Riera, G., Aromí, G. & Sañudo, E. C. Magnetic molecules on surfaces: SMMs and beyond. *Coordination Chemistry Reviews* **475**, 214858 (2023).
32. Berti, G. *et al.* Scanning tunneling microscopy and spectroscopy characterization of Nb films for quantum applications. *Applied Physics Letters* **122** (2023).
33. Wang, Y. *et al.* Universal quantum control of an atomic spin qubit on a surface. *npj Quantum Information* **9**, 48 (2023).
34. Ghirri, A. *et al.* Self-assembled monolayer of Cr7Ni molecular nanomagnets by sublimation. *ACS nano* **5**, 7090–7099 (2011).
35. Vaxevani, K. *et al.* Extending the spin excitation lifetime of a magnetic molecule on a proximitized superconductor. *Nano Letters* **22**, 6075–6082 (2022).
36. *Sonnet User's Guide, Release 18* <https://www.sonnetsoftware.com/support>.
37. Probst, S., Song, F., Bushev, P. A., Ustinov, A. V. & Weides, M. Efficient and robust analysis of complex scattering data under noise in microwave resonators. *Review of Scientific Instruments* **86** (2015).
38. Barends, R. *et al.* Frequency and quality factor of NbTiN/Au bilayer superconducting resonators. **1185**, 152–155 (2009).
39. Day, P. K., LeDuc, H. G., Mazin, B. A., Vayonakis, A. & Zmuidzinas, J. A broadband superconducting detector suitable for use in large arrays. *Nature* **425**, 817–821 (2003).
40. Mattis, D. C. & Bardeen, J. Theory of the anomalous skin effect in normal and superconducting metals. *Physical Review* **111**, 412 (1958).
41. Zmuidzinas, J. Superconducting microresonators: Physics and applications. *Annu. Rev. Condens. Matter Phys.* **3**, 169–214 (2012).
42. Burnett, J., Sagar, J., Kennedy, O. W., Warburton, P. A. & Fenton, J. C. Low-loss superconducting nanowire circuits using a neon focused ion beam. *Physical Review Applied* **8**, 014039 (2017).
43. Frasca, S. *et al.* NbN films with high kinetic inductance for high-quality compact superconducting resonators. *Physical Review Applied* **20**, 044021 (2023).
44. Swenson, L. *et al.* Operation of a titanium nitride superconducting microresonator detector in the nonlinear regime. *Journal of Applied Physics* **113** (2013).
45. Andersson, G. *et al.* Acoustic spectral hole-burning in a two-level system ensemble. *npj Quantum Information* **7**, 15 (2021).